

## Topical Review

# Antimony selenide thin-film solar cells

Kai Zeng, Ding-Jiang Xue and Jiang Tang

Wuhan National Laboratory for Optoelectronics (WNLO) and School of Optical and Electronic Information, Huazhong University of Science and Technology, Wuhan, 430074, Hubei, People's Republic of China

E-mail: [jtang@mail.hust.edu.cn](mailto:jtang@mail.hust.edu.cn)

Received 27 March 2015, revised 21 March 2016

Accepted for publication 24 March 2016

Published 19 April 2016

**Abstract**

Due to their promising applications in low-cost, flexible and high-efficiency photovoltaics, there has been a booming exploration of thin-film solar cells using new absorber materials such as  $\text{Sb}_2\text{Se}_3$ ,  $\text{SnS}$ ,  $\text{FeS}_2$ ,  $\text{CuSbS}_2$  and  $\text{CuSbSe}_2$ . Among them,  $\text{Sb}_2\text{Se}_3$ -based solar cells are a viable prospect because of their suitable band gap, high absorption coefficient, excellent electronic properties, non-toxicity, low cost, earth-abundant constituents, and intrinsically benign grain boundaries, if suitably oriented. This review surveys the recent development of  $\text{Sb}_2\text{Se}_3$ -based solar cells with special emphasis on the material and optoelectronic properties of  $\text{Sb}_2\text{Se}_3$ , the solution-based and vacuum-based fabrication process and the recent progress of  $\text{Sb}_2\text{Se}_3$ -sensitized and  $\text{Sb}_2\text{Se}_3$  thin-film solar cells. A brief overview further addresses some of the future challenges to achieve low-cost, environmentally-friendly and high-efficiency  $\text{Sb}_2\text{Se}_3$  solar cells.

Keywords:  $\text{Sb}_2\text{Se}_3$ , thin film, solar cell, thermal evaporation, grain boundary

(Some figures may appear in colour only in the online journal)

**1. Introduction**

Copper indium gallium selenide (CIGS) and cadmium telluride (CdTe), the most representative thin-film solar cells (TFSCs), have achieved energy conversion efficiencies of 21.7% [1] and 21.5% [2], respectively. However, the high cost of In and Ga and the toxicity of Cd are both unavoidable factors that reduce the commercial competitiveness of CIGS and CdTe solar cells. Copper zinc tin sulfoselenide (CZTSSe) is a recent research hotspot for thin-film photovoltaics and has achieved an efficiency of 12.6% [3]. Unfortunately, the rigorous phase and composition control make the fabrication process extremely demanding and complicated, thus obstructing its further efficiency growth. Other potential absorber materials like  $\text{SnS}$  [4],  $\text{CuSbS}_2$  [5, 6],  $\text{CuSbSe}_2$  [7] and  $\text{FeS}_2$  [8] have long been investigated, but the efficiencies remain too low and unsatisfactory.

Ever since first reported by Miyasaka *et al* in 2006, perovskite solar cells have attracted the interest of scientists around the world. Device efficiency increased from 3.8% [9] to 20.1% [10] in 2015 with a ramp rate never seen before. Inorganic–organic lead iodide perovskite in general and

$\text{CH}_3\text{NH}_3\text{PbI}_3$  in particular, possess excellent properties such as a decent band gap of 1.55 eV, a strong absorption coefficient and long electron/hole diffusion lengths ( $>1\text{ }\mu\text{m}$  [11]) enabled by the long carrier lifetime and decent carrier mobility, thus ensuring an appreciable photovoltaic efficiency. The toxicity of Pb and its intrinsic instability, however, are tough issues that set barriers on its further commercialization. Hence, a search for new, stable and low-toxic materials for efficient thin-film photovoltaics is necessary. This review will focus on  $\text{Sb}_2\text{Se}_3$ , a material that almost satisfies all the criteria.

**2. Properties of  $\text{Sb}_2\text{Se}_3$** 

$\text{Sb}_2\text{Se}_3$  is in the family of binary  $\text{V}_2\text{-VI}_3$  compounds ( $\text{Bi}_2\text{S}_3$ ,  $\text{Bi}_2\text{Se}_3$ ,  $\text{Bi}_2\text{Te}_3$ ,  $\text{Sb}_2\text{Se}_3$ ,  $\text{Sb}_2\text{Te}_3$ ...), which are reported to have diverse properties such as thermoelectricity [12], topological insulativity [13] and superconductivity [14]. Few of them were reported for application in photovoltaics, except  $\text{Sb}_2\text{Se}_3$  on which our group has worked extensively for thin-film solar cells. In this section, we will review the basic

**Table 1.** Material properties of  $\text{Sb}_2\text{Se}_3$ .

Property		Value	Reference
Crystal lattice	$a(\text{\AA})$	11.6330	[15]
	$b(\text{\AA})$	11.7800	
	$c(\text{\AA})$	3.9850	
Density( $\text{g cm}^{-3}$ )		5.84	[16]
Space group		Pnma 62	[15]
Melting point(K)		885	[16]
Band gap(eV)	direct	1.17 (300 K)	[17]
	indirect	1.03 (300 K)	
Absorption coefficient( $\text{cm}^{-1}$ )		$>10^5$	[17, 18]
Relative dielectric constant		15	[16]
Mobility	$\mu_e(\text{cm}^2 \cdot \text{V}^{-1} \cdot \text{s}^{-1})$	15	[16]
	$\mu_p(\text{cm}^2 \cdot \text{V}^{-1} \cdot \text{s}^{-1})$	42	

material and optoelectronic properties of  $\text{Sb}_2\text{Se}_3$ . We begin with table 1 which summarizes the crystal lattice parameters, band gap, mobility, etc, of  $\text{Sb}_2\text{Se}_3$ .

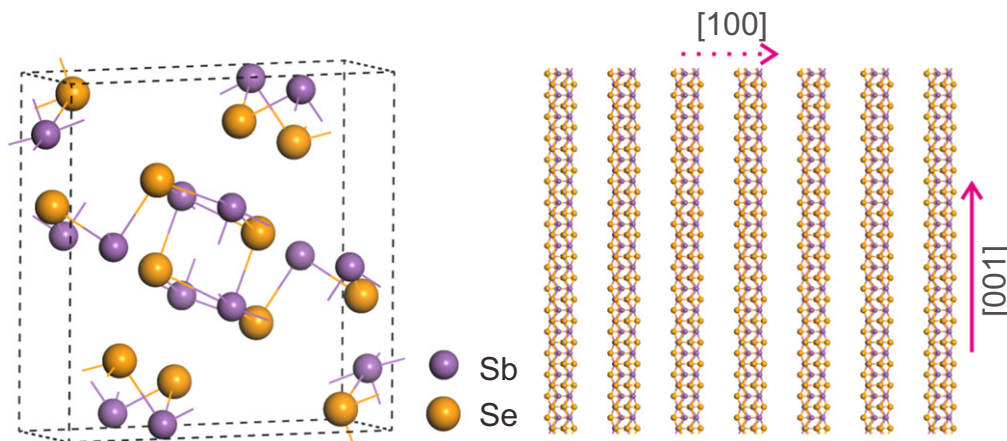
### 2.1. Material properties

$\text{Sb}_2\text{Se}_3$  is an inorganic binary compound existing naturally in the form of stibnite.  $\text{Sb}_2\text{Se}_3$  has an orthorhombic crystal structure and a space group of Pnma 62, with lattice constants  $a = 11.6330 \text{ \AA}$ ,  $b = 11.7800 \text{ \AA}$ ,  $c = 3.9850 \text{ \AA}$  and a primitive cell volume of  $0.524 \text{ nm}^3$ . As a material composed of 1D ribbons, the  $[\text{Sb}_4\text{Se}_6]_n$  ribbons are accumulated through van der Waals forces along  $a$  and  $b$  axes, whereas inside the  $[\text{Sb}_4\text{Se}_6]_n$  nanoribbon strong covalent bonds exist. Within the  $[\text{Sb}_4\text{Se}_6]_n$  ribbons trigonal  $\text{Sb}_1\text{Se}_2\text{Se}_3$  and tetragonal  $\text{Sb}_1\text{Se}_2\text{Se}_3$  link alternately. As a simple binary compound,  $\text{Sb}_2\text{Se}_3$  has only an orthorhombic phase at normal temperature and pressure, thus avoiding the complexity of composition and phase control. The melting point of  $\text{Sb}_2\text{Se}_3$  is 885 K, far lower than that of CdTe (1366 K). Reported experimental data reveal that  $\text{Sb}_2\text{Se}_3$  crystals can be obtained at micron size when sintered at  $300^\circ\text{C}$ – $400^\circ\text{C}$ , implying the possibility of building flexible solar cells on polyimide (PI) substrate. The raw material of  $\text{Sb}_2\text{Se}_3$  is low-toxic, earth-abundant and

relatively inexpensive. Despite no data being available in LD50 or LCT50 to describe the toxicity of  $\text{Sb}_2\text{Se}_3$ , it is still believed that  $\text{Sb}_2\text{Se}_3$  is of low toxicity as a result of its absence from the list of highly toxic or carcinogenic materials by Chinese, American or European Union regulation authorities. The elemental abundance of Sb and Se in the Earth's crust are 0.2 and 0.05 ppm, respectively, higher than those of In (0.049 ppm) and Te (0.005 ppm), making it possible for the manufacturing of solar cells at a level of 100 GW. Meanwhile, according to the London Metal Exchange, the buying rates of Sb and Se are approximately  $\$5.3/\text{kg}$  and  $\$19.4/\text{kg}$ , respectively, far lower than those of In ( $\$280/\text{kg}$ ) and Te ( $\$35/\text{kg}$ ). As a consequence, the cost of the raw material is only 5 cents for depositing a  $1 \text{ m}^2$   $\text{Sb}_2\text{Se}_3$  thin film at a film thickness of  $1 \text{ }\mu\text{m}$ .

### 2.2. Optical properties

We then describe the attractive optoelectronic properties of  $\text{Sb}_2\text{Se}_3$  relating to photovoltaic application.  $\text{Sb}_2\text{Se}_3$  is generally reported as an indirect-band-gap semiconductor with a band gap of  $1.0$ – $1.2 \text{ eV}$  [17]. The direct and indirect band gaps at room temperature are 1.17 and 1.03 eV, respectively, tested by our group using the temperature-dependent transmission spectrum (TDTS), as shown in figure 2. Calculated by the Shockly–Queisser theory [18], the theoretical solar conversion efficiency of a single-junction solar cell can reach up to 30%. The absorption coefficient of bulk  $\text{Sb}_2\text{Se}_3$  is larger than  $10^5 \text{ cm}^{-1}$  in ultraviolet and visible spectrum, allowing sufficient absorption of the solar spectrum within a 500 nm thin film. The complex refractive index ( $N = n + ik$ , where  $N$  is the complex refractive index;  $n$  is the refractive index; and  $k$  is the extinction coefficient) of a- $\text{Sb}_2\text{Se}_3$  and c- $\text{Sb}_2\text{Se}_3$  film was then tested using an ellipsometer (J. A. Woollam, RC2). The measured refractive index and extinction coefficient of a- $\text{Sb}_2\text{Se}_3$  ( $n_a$ ,  $k_a$ ) and c- $\text{Sb}_2\text{Se}_3$  ( $n_c$ ,  $k_c$ ) are shown in figure 3(a). The dielectric constant related to dielectric polarization and exciton binding energy is an essential parameter in semiconductors. The complex relative dielectric constant could be described as  $\varepsilon' = n^2 - k^2$ ,  $\varepsilon'' = 2nk$ , where

**Figure 1.** Crystal structure of  $\text{Sb}_2\text{Se}_3$ .

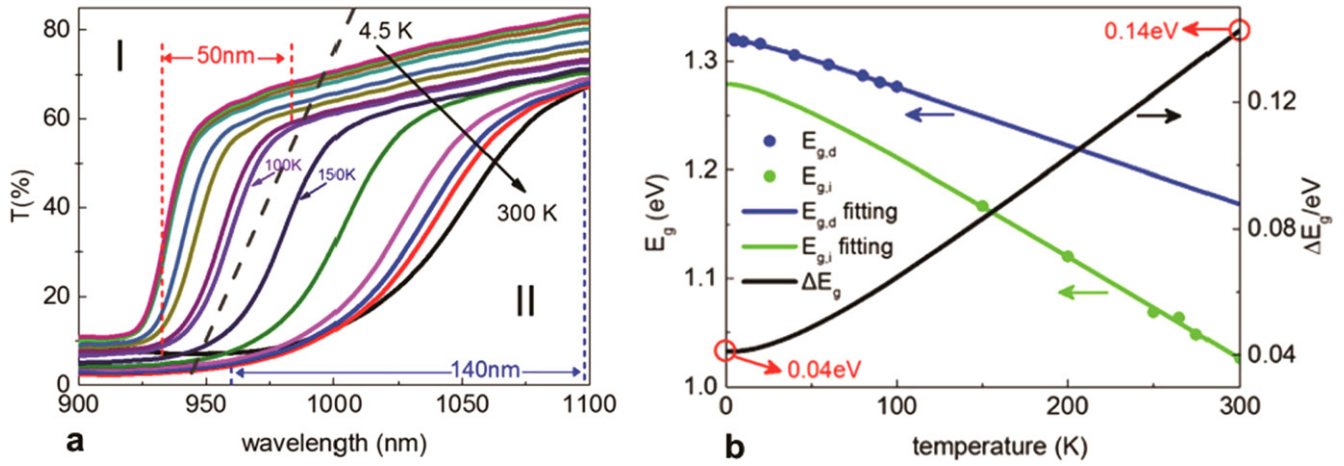


**Figure 2.** (a) Temperature-dependent transmission spectrum of crystalline-Sb<sub>2</sub>Se<sub>3</sub> thin films. The measured temperature was in the order of 4.5–300 K. (b) Temperature-dependent band gap of c-Sb<sub>2</sub>Se<sub>3</sub>. The solid points are the experimental band gaps at different temperatures, and the solid blue and green lines are the corresponding fitting curves for direct band gap ( $E_{g,d}$ ) and indirect band gap ( $E_{g,i}$ ), respectively. The dark line is the difference between  $E_{g,d}$  and  $E_{g,i}$ . (Reprinted with permission from reference [17]. Copyright 2015 AIP Publishing LLC).

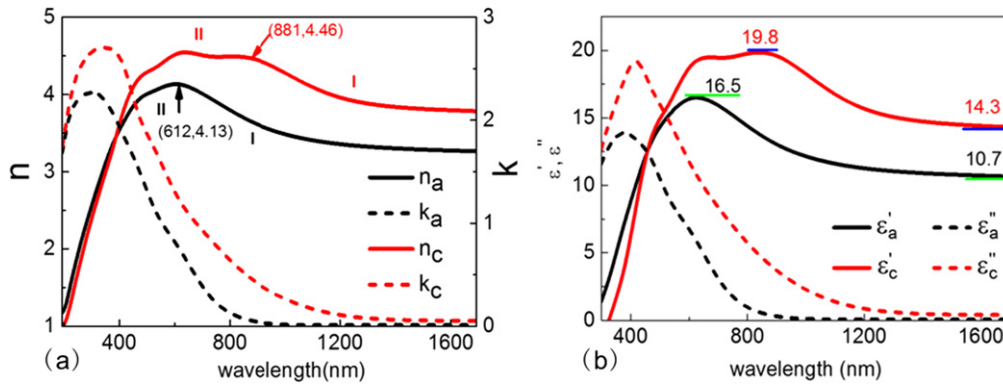


**Figure 3.** (a) The refractive index and extinction coefficient of a-Sb<sub>2</sub>Se<sub>3</sub> and c-Sb<sub>2</sub>Se<sub>3</sub> films measured by ellipsometry in the wavelength range of 193–1693 nm. (b) The complex dielectric constant of a-Sb<sub>2</sub>Se<sub>3</sub> and c-Sb<sub>2</sub>Se<sub>3</sub> films versus photon wavelength. The blue and green short solid lines mark the typical values of the real part of the relative dielectric constant. (Reprinted with permission from reference [17]. Copyright 2015 AIP Publishing LLC).

$\epsilon'$  and  $\epsilon''$  are the real and imaginary parts of the complex relative dielectric constant, respectively, shown in figure 3(b).

### 2.3. Electrical properties

Thin-film Sb<sub>2</sub>Se<sub>3</sub> normally exhibits p-type conductivity. Its electron mobility is determined to be  $15 \text{ cm}^2 \cdot \text{V}^{-1} \cdot \text{s}^{-1}$ , and the hole mobility is  $42 \text{ cm}^2 \cdot \text{V}^{-1} \cdot \text{s}^{-1}$  [16], comparable with that of CdTe ( $\mu_p = 60 \text{ cm}^2 \cdot \text{V}^{-1} \cdot \text{s}^{-1}$ ). Moreover, its dielectric constant is relatively larger (14.3–19.8, previously described in figure 3(b)) compared with CIGS ( $\epsilon = 13.6$ ) and CdTe ( $\epsilon = 7.1$ ), which leads to a lower exciton binding energy that implies an immediate separation of electrons and holes upon photogeneration. Similarly, the depth of defects should also be relatively lower due to its inverse proportion to the square of the relative dielectric constant. Under these conditions, the recombination loss caused by the defects drops considerably, leading to a higher possible power conversion efficiency (PCE).

### 2.4. Defect properties

As shown in figure 1, Sb<sub>2</sub>Se<sub>3</sub> possesses a unique 1D crystal structure that differs from most traditional inorganic solar-cell materials with a 3D crystal structure such as Si, GaAs and ZnO. In the orthogonal direction, the parallel-stacked ribbons would substantially provide no dangling bonds, even at grain boundaries (GBs), and probably minimize recombination losses, as shown in figure 4(a). First-principles simulations [19] confirm that, as long as the Sb<sub>2</sub>Se<sub>3</sub> ribbons are suitably *c*-axis oriented, the GBs will be terminated by the intrinsically inert surfaces (for example, (100), (010), (110) and (120) planes) and the recombination loss is thus minimized as shown in figure 4(b). For most known photovoltaic absorbers possessing 3D crystal structure, the breakage of covalent bonds inevitably introduces defect states and recombination centers at the GBs and thus requires post-treatment to remedy this problem. These intrinsically benign GBs endow Sb<sub>2</sub>Se<sub>3</sub> with an important



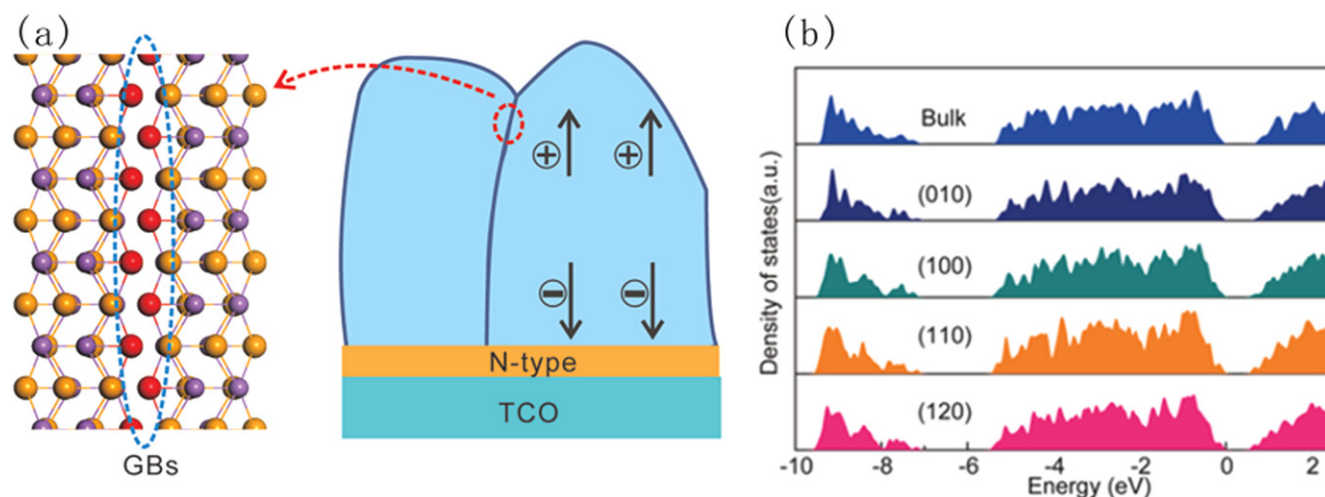


**Figure 4.** (a) All the atoms at the edge of [001] ribbons are saturated (highlighted as red spheres) and introduce no recombination loss at the GBs once they are oriented vertically onto the substrates. (b) The density of states (DOS) of the bulk  $\text{Sb}_2\text{Se}_3$  and of four surfaces that are parallel to the [001] direction. The forbidden gap is the empty zone near 0 eV. (Reprinted with permission from Macmillan Publishers Ltd: *Nature* [19]. Copyright 2015).

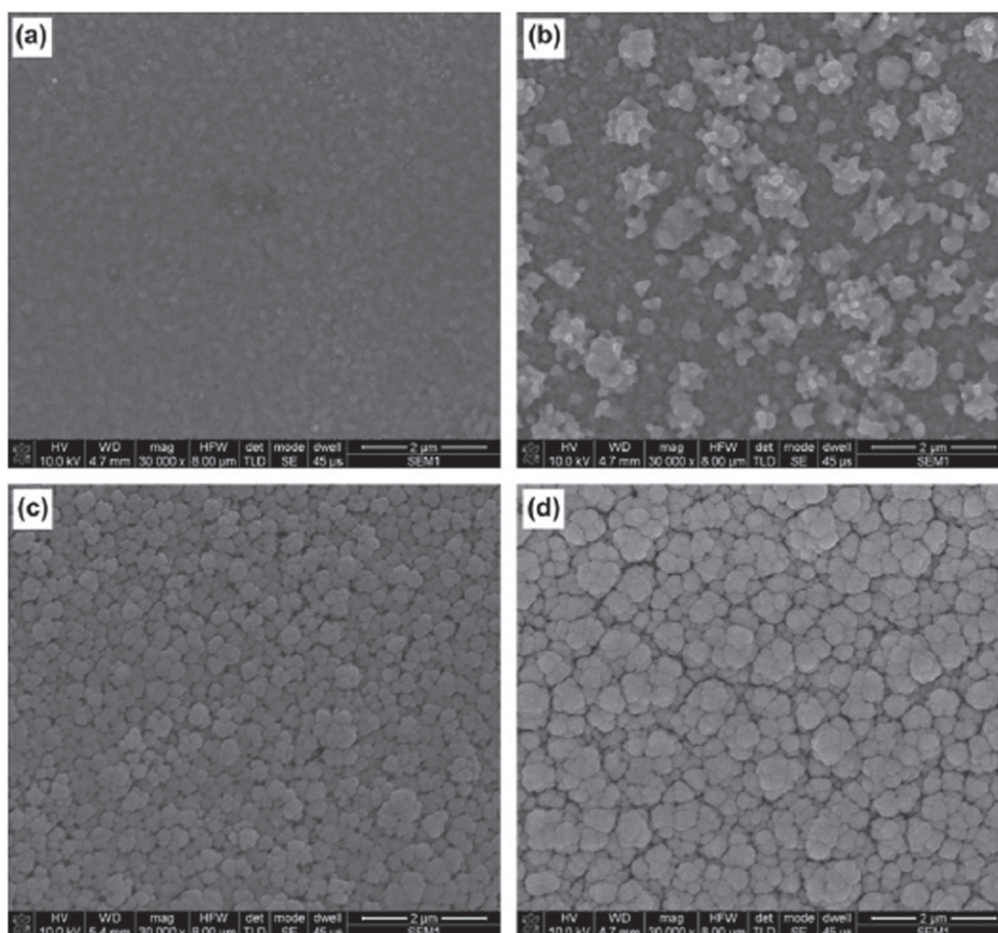


**Figure 5.** Surface morphologies of antimony selenide thin films deposited at 25 °C and different potentials: (a) -0.4 V, (b) -0.5 V, (c) -0.55 V, (d) -0.6 V. Film thickness ranges from 1.05 to 1.17 μm. (Reprinted from reference [26]. Copyright 2012, with permission from Elsevier).

advantage in photovoltaic applications, because recombination losses at GBs are one of the major limiting factors for high-efficiency thin-film solar cells.

Collectively,  $\text{Sb}_2\text{Se}_3$  has a fixed phase, suitable band gap, strong absorption coefficient, low-crystallization temperature, intrinsically benign GBs, low toxicity and low-cost

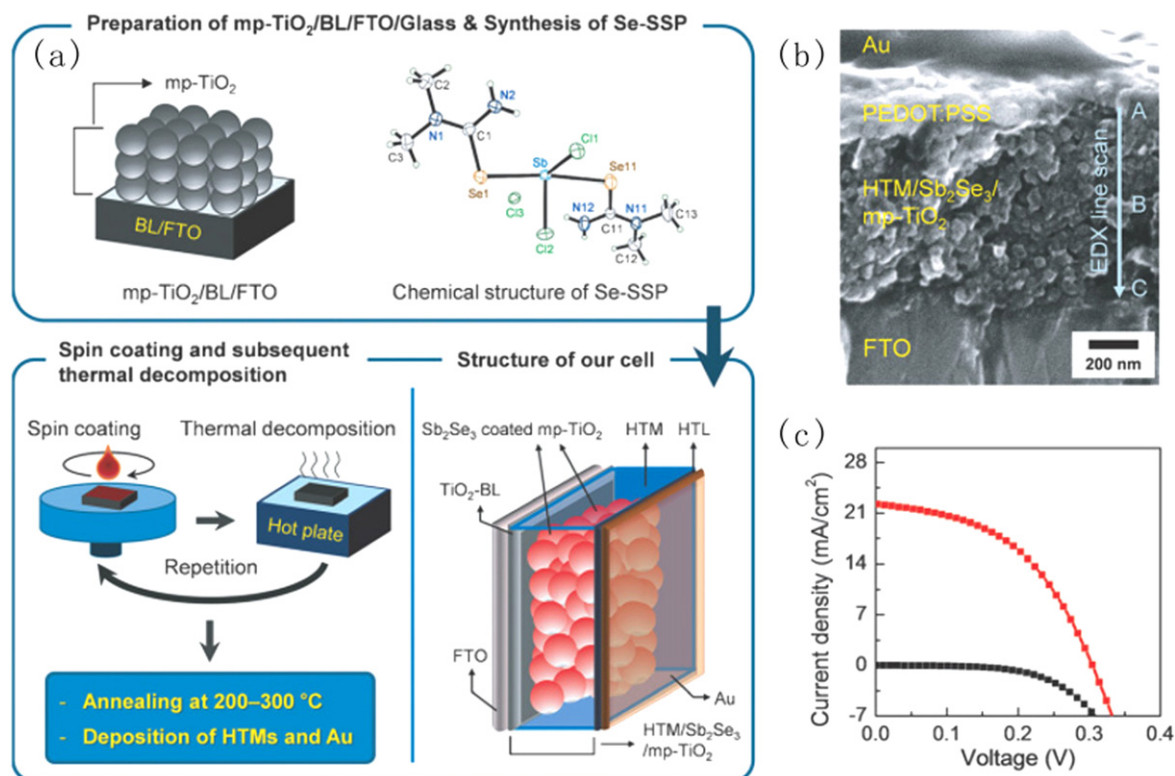


**Figure 6.** (a) The fabrication process for Sb<sub>2</sub>Se<sub>3</sub>-sensitized inorganic–organic heterojunction cells. (b) Cross-sectional FESEM image of the final cells. (c) Density–voltage ( $J$ – $V$ ) characteristics under light (red line) and dark (black line) conditions. (Reprinted with permission from reference [27]. Copyright 2013 John Wiley and Sons).

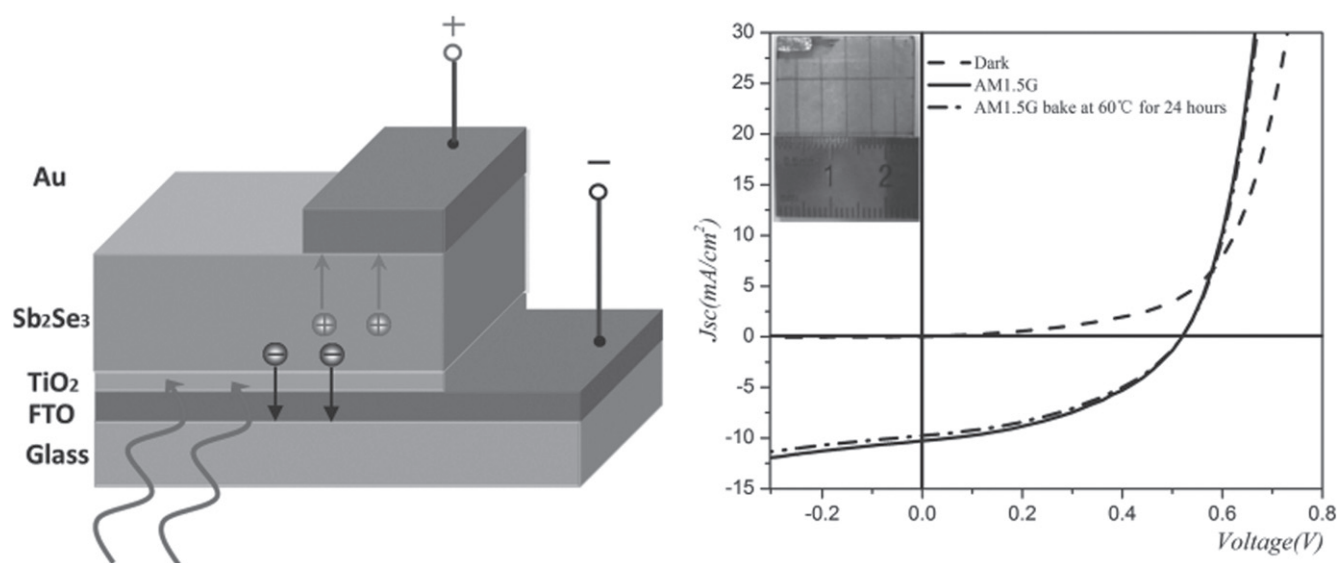


**Figure 7.** Schematic configuration of Sb<sub>2</sub>Se<sub>3</sub>/TiO<sub>2</sub> heterojunction device and  $J$ – $V$  characteristics of Sb<sub>2</sub>Se<sub>3</sub> solar-cell performance. (Reprinted with permission from reference [15]. Copyright 2014 John Wiley and Sons).

constituents. All these features merit its exploration for high-efficiency, low-cost thin-film solar cells [20].

### 3. Thin-film Sb<sub>2</sub>Se<sub>3</sub> fabrication

Since Sb<sub>2</sub>Se<sub>3</sub> has great potential in photovoltaics, related studies are conducted on its material properties and

fabrication process. The synthesis and characterization of nanostructured Sb<sub>2</sub>Se<sub>3</sub> and Sb<sub>2</sub>Se<sub>3</sub> thin film were extensively explored in the literature, but with few reports on the study of its photovoltaic device performance. Muscat *et al* [21] synthesized Sb<sub>2</sub>Se<sub>3</sub> and Sb<sub>2</sub>(Se, S)<sub>3</sub> alloy nanotubes using the hot injection method in 2009. The obtained single-crystal nanotubes have tunable composition, orthorhombic phase, well-defined rectangular cross sections, and growth direction along

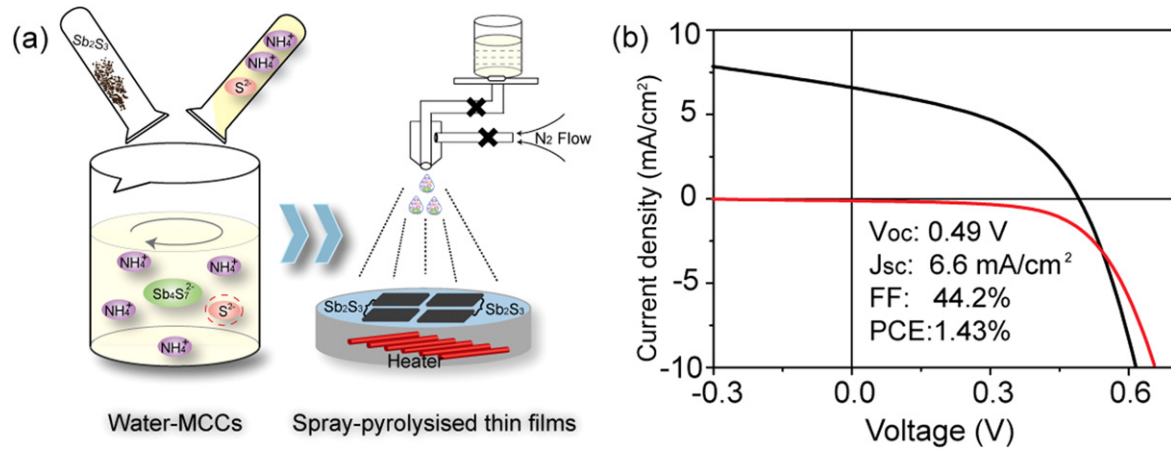


**Figure 8.** (a) Schematic illustration for the synthesis and application of water-MCCs. (b)  $J$ - $V$  characteristics of  $\text{Sb}_2(\text{S}_{0.44}, \text{Se}_{0.56})_3$  device performance in the dark and under  $100 \text{ mW cm}^{-2}$  simulated AM1.5G irradiation. (Reprinted with permission from reference [30]. Copyright 2015 American Chemical Society).

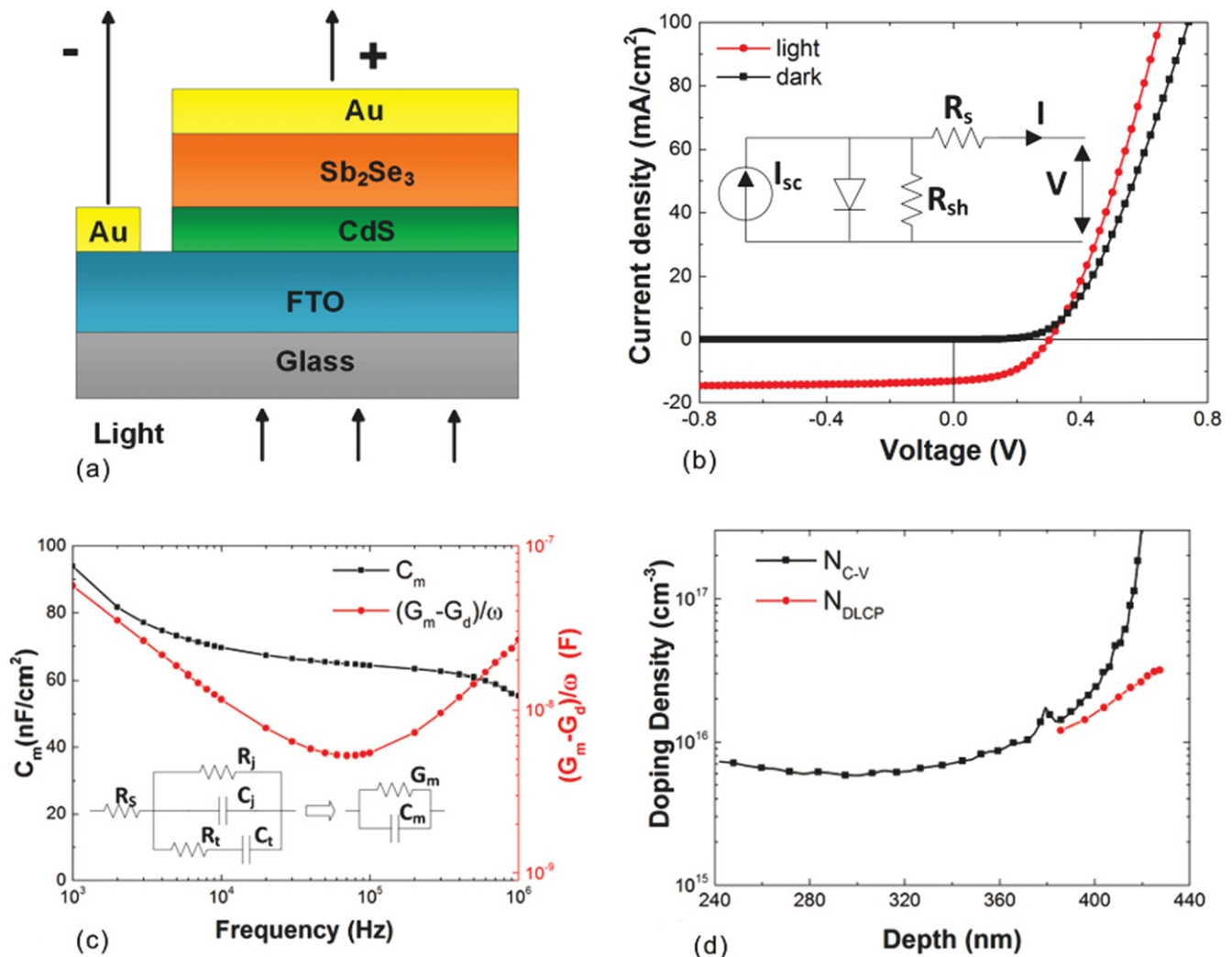


**Figure 9.** Schematic superstrate  $\text{Sb}_2\text{Se}_3$  photovoltaic device (a) and  $J$ - $V$  curves and simplified diode circuit model (b) and C-f (c), C-V and DLCP (d) characterization. (Reprinted with permission from reference [32]. Copyright 2014, AIP Publishing LLC).

[001]. Golberg *et al* [22] synthesized single-crystalline  $\text{Sb}_2\text{Se}_3$  nanowires using a hydrothermal method and investigated its field emission and photoconductive properties.

Field-emission measurements showed that the nanostructures have a low turn-on field of  $2.6 \text{ V } \mu\text{m}^{-1}$  at a current density of  $10 \text{ } \mu\text{A cm}^{-2}$ , a low threshold field of  $4.9 \text{ V } \mu\text{m}^{-1}$  at a current



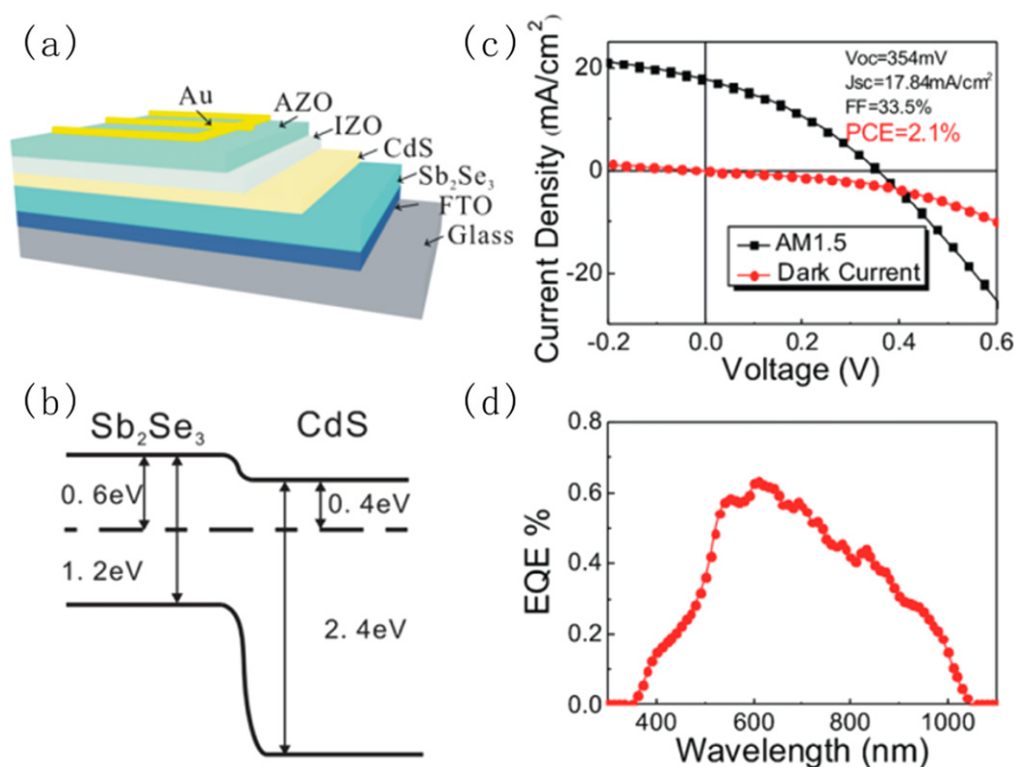


**Figure 10.** (a) Schematic demonstration of the device configuration, (b) sketchy band diagram, (c) dark and light current density curves, and (d) EQE spectrum of  $\text{Sb}_2\text{Se}_3$  solar cell. (Reprinted with permission from reference [33]. Copyright 2014 American Chemical Society).

density of  $1 \text{ mA cm}^{-2}$  and a high enhancement factor of 3466. The individual  $\text{Sb}_2\text{Se}_3$  nanowire photodetectors exhibited a marked response to visible light (spectral responsivity ( $R_\lambda$ ) and external quantum efficiency (EQE) are as high as  $\sim 8.0 \text{ A W}^{-1}$  and  $\sim 1650\%$ , with a response time of less than 0.3 s).

In respect to thin film, there are different deposition methods reported. Two different Se sources ( $\text{SeO}_2$  and  $\text{CSe}(\text{NH}_2)_2$ ) were used to spray-deposit  $\text{Sb}_2\text{Se}_3$  thin films by Bhosale *et al* [23]. XRD patterns revealed that  $\text{Sb}_2\text{Se}_3$  films prepared using  $\text{SeO}_2$  as a Se source are amorphous, while those prepared using  $\text{CSe}(\text{NH}_2)_2$  are polycrystalline with orthorhombic crystal structure. El-Sayad *et al* [24] obtained amorphous  $\text{Sb}_2\text{Se}_3$  and  $\text{Sb}_2(\text{S}, \text{Se})_3$  alloy films using the thermal evaporation process (TE) in 2008. The as-prepared films were amorphous when annealed at  $T_a < 423 \text{ K}$ . From the interference and interference-free transmittance data, the optical constants and consequently the dispersion parameters of the indicated films were determined. In 2012, Haque *et al* [25] prepared  $\text{Sb}_2\text{Se}_3$  nanocrystals on mesoporous  $\text{TiO}_2$  substrate using successive ionic layer adsorption and reaction (SILAR), with Se and  $\text{NaBH}_4$  solution in ethanol as the selenium source and  $\text{SbCl}_3$  solution in acetone as the antimony source. Transient absorption spectroscopy studies reveal an efficient charge separation yield at the spiro-OMe-TAD/ $\text{Sb}_2\text{Se}_3$ / $\text{TiO}_2$  heterojunction with an electron-hole recombination lifetime of 50 ms, suggesting that  $\text{Sb}_2\text{Se}_3$  is also a promising candidate in sensitized solar cells. And in the same year, Lai *et al* [26] prepared  $\text{Sb}_2\text{Se}_3$  thin film by potentiostatic electrodeposition from an aqueous acid bath

containing  $\text{K}(\text{SbO})\text{C}_4\text{H}_4\text{O}_6 \cdot 0.5\text{H}_2\text{O}$  and  $\text{H}_2\text{SeO}_3$  at  $25^\circ\text{C}$ . Scanning electron microscope (SEM) images of the products are shown in figure 5 for different electrodeposition potentials. The various methods reported for the fabrication of  $\text{Sb}_2\text{Se}_3$  nanostructures and films lay the foundation for their photovoltaic application.

## 4. Recent progress in $\text{Sb}_2\text{Se}_3$ -based solar cells

In the solar cell field,  $\text{Sb}_2\text{Se}_3$  is generally applied in sensitized solar cells as a sensitizer and in planar thin-film solar cells as an absorber layer. Both structures have achieved impressive enhancement in performance and illustrated great potential.

### 4.1. $\text{Sb}_2\text{Se}_3$ -sensitized solar cells

Since antimony trisulfide ( $\text{Sb}_2\text{S}_3$ ) is widely used as a successful light sensitizer for efficient inorganic-organic heterojunction solar cells,  $\text{Sb}_2\text{Se}_3$  is then introduced to replace  $\text{Sb}_2\text{S}_3$  for its proper band gap and large absorption coefficient.

In 2014, Seok *et al* [27] deposited  $\text{Sb}_2\text{Se}_3$  on mesoporous  $\text{TiO}_2$  utilizing multiple cycles of spin coating with a Se single-source precursor solution and thermal decomposition, followed by annealing at  $300^\circ\text{C}$  in Ar atmosphere, as shown in figure 6(a). The cross-section image in figure 6(b) further shows the structure and the thickness of the as-prepared device. The most efficient solar cell with a structure of FTO/bulk- $\text{TiO}_2$ /mp- $\text{TiO}_2$ / $\text{Sb}_2\text{Se}_3$ /HTM/HTL/Au was fabricated and yielded a PCE of 3.21% shown in figure 6(c), where

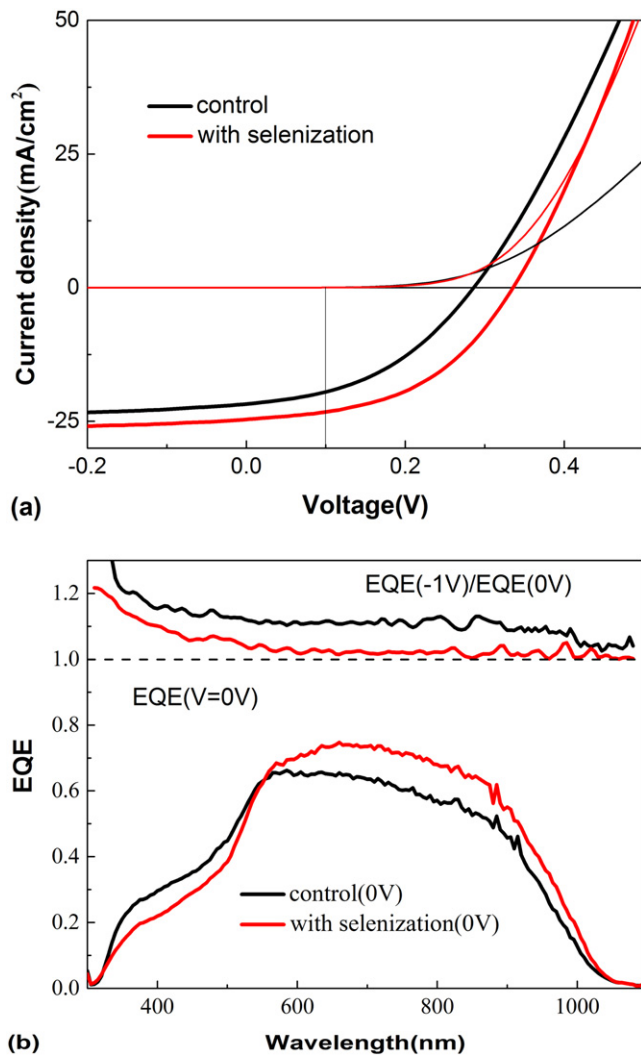


**Figure 11.**  $J$ - $V$  (a) and EQE (b) characteristics of  $\text{Sb}_2\text{Se}_3$  solar cells with/without selenization. (Reprinted with permission from reference [34]. Copyright 2014, AIP Publishing LLC).

HTM stands for hole-transporting materials (poly[2,6-(4,4-bis(2-ethylhexyl)-4H-cyclopenta[2,1-b;3,4-b']dithiophene)-alt-4,7-(2,1,3-benzothiadiazole)], PCPDTBT) and HTL stands for hole-transporting layers (Poly(3,4-ethylenedioxythiophene):poly(styrene sulfonate), PEDOT:PSS). The cell presented herein is the first of its kind to use  $\text{Sb}_2\text{Se}_3$  as an effective light sensitizer, and its capability of expanding the absorption spectrum to the near-IR region up to 1050 nm was demonstrated.

To diminish the  $V_{oc}$  and PCE loss in the sensitized solar cells,  $\text{Sb}_2(\text{S},\text{Se})_3$  alloy was then used to replace  $\text{Sb}_2\text{Se}_3$  [28]. The alloy can be formed because  $\text{Sb}_2\text{Se}_3$  and  $\text{Sb}_2\text{S}_3$  compounds are isomorphous semiconductors both showing orthorhombic crystal structure. The combination of  $\text{Sb}_2\text{Se}_3$  and  $\text{Sb}_2\text{S}_3$  can be an effective approach to extend the light-harvesting properties up to the near-IR region for a higher  $J_{sc}$  than the  $\text{Sb}_2\text{S}_3$ -sensitized solar cells. Solar cells based on the  $\text{Sb}_2\text{Se}_3$ -modified  $\text{Sb}_2\text{S}_3$  sensitizer exhibit the highest PCE of 6.6% with a very high  $J_{sc}$  of  $24.9 \text{ mA cm}^{-2}$ ,  $V_{oc}$  of 474.8 mV and  $FF$  of 55.6%, compared to pristine  $\text{Sb}_2\text{S}_3$ - and  $\text{Sb}_2\text{Se}_3$ -based cells. Through absorption spectrum and EQE

measurement the broader spectrum for light harvesting is confirmed. The graded composition by sequential deposition of  $\text{Sb}_2\text{Se}_3$  and  $\text{Sb}_2\text{S}_3$  for the mp- $\text{TiO}_2/\text{Sb}_2\text{Se}_3/\text{Sb}_2\text{S}_3$ -based cell provides a cascaded band alignment, allowing sufficient charge transport. Around the same year, Tena-Zaera *et al* [29] fabricated a FTO/ $\text{TiO}_2/\text{Sb}_2\text{Se}_3/\text{CuSCN}/\text{Au}$  planar sensitized solar cell using electrodeposited  $\text{Sb}_2\text{Se}_3$  and achieved a device efficiency of 2.1%. The effect of the  $\text{Sb}_2\text{Se}_3$  thickness and microstructural properties on the photocurrent is analyzed, suggesting the hole transport is the main limiting mechanism. In all these reports, no device stability is discussed, which is an important parameter for any type of solar cell when its potential for real application is evaluated.

#### 4.2. $\text{Sb}_2\text{Se}_3$ thin-film solar cells

**4.2.1. Solution process method.** Solution deposition of antimony selenium containing chalcogenide seemed to be first introduced by Nair *et al* [31] in 2009. They applied a chemical bath deposition (CBD) method to obtain  $\text{Sb}_2\text{Se}_{3-x}\text{S}_x:\text{Sb}_2\text{O}_3$  absorber layer and subsequently built a TCO/ $\text{CdS}/\text{Sb}_2\text{Se}_{3-x}\text{S}_x:\text{Sb}_2\text{O}_3/\text{PbS}$  solar cell. The all-chemically deposited thin-film solar cell has a  $V_{oc}$  of 520 mV, a  $J_{sc}$  of  $4.2 \text{ mA cm}^{-2}$  and a PCE of 0.66%, while its scalability is demonstrated in four series-connected cells of area  $1 \text{ cm}^2$  each, showing  $J_{sc}$  of  $1.5 \text{ mA cm}^{-2}$  and  $V_{oc}$  of 1.9 V under sunlight. Despite this, they produced an antimony sulfoselenide and antimony oxide mixture by the CBD method. This work is very stimulating.

Our group worked extensively in  $\text{Sb}_2\text{Se}_3$  photovoltaics with special emphasis on  $\text{Sb}_2\text{Se}_3$  thin-film solar cells from the very beginning. In 2014, we reported a hydrazine ( $\text{N}_2\text{H}_4$ ) solution method [15] to deposit  $\text{Sb}_2\text{Se}_3$  thin film on classical  $\text{TiO}_2$  buffer layer to build a heterojunction  $\text{TiO}_2/\text{Sb}_2\text{Se}_3$  solar cell. The band position measured from cyclic voltammetry allows an optimal band offset with  $\text{TiO}_2$  to form a type-II staggered heterojunction, while  $\text{TiO}_2$  is non-toxic, stable and nonreactive, and has few structural defects and recombination centers at the interface. Based on a  $\text{Sb}_2\text{Se}_3/\text{TiO}_2$  superstrate structure, the heterojunction solar cell achieved a device efficiency of 2.26% ( $V_{oc} = 0.52 \text{ V}$ ,  $J_{sc} = 10.3 \text{ mA}$ ,  $FF = 42.3\%$ ), as shown in figure 7. The device showed such good stability that little efficiency drop (0.11%) was observed after being baked at  $60^\circ\text{C}$  for 24 h.

To avoid the toxicity of hydrazine and possible danger during the fabrication process, recently our group presented a versatile and environmentally benign water-based solution method [30] for the preparation of various metal chalcogenide complexes (MCCs) through directly dissolving a series of bulk  $\text{V}_2\text{-VI}_3$  chalcogenides ( $\text{V} = \text{Sb, As}$  and  $\text{VI} = \text{S, Se, Te}$ ) in water with the presence of  $(\text{NH}_4)_2\text{S}$  at room temperature and ambient atmosphere. We showed that such water-MCCs could be readily processed into corresponding semiconducting thin films, which is shown in figure 8(a). Subsequently, we chose  $\text{Sb}_2(\text{S}_{0.44}, \text{Se}_{0.56})_3$  film as an example to fabricate heterojunction solar cells with the structure of glass/FTO/ $\text{TiO}_2/\text{Sb}_2(\text{S}_{0.44}, \text{Se}_{0.56})_3/\text{Au}$ . Figure 8(b) shows the current density versus voltage ( $J$ - $V$ ) characteristics of the device



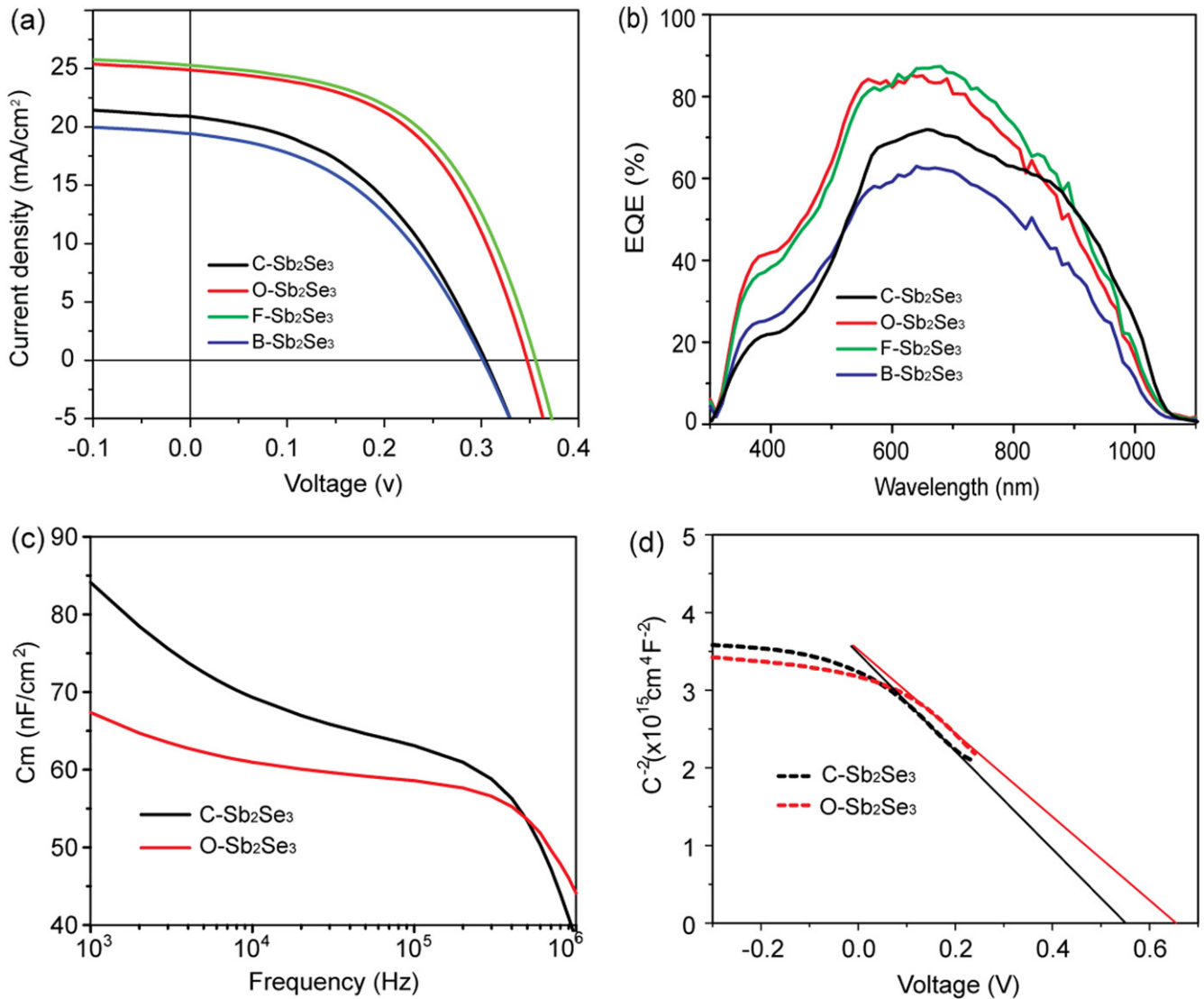


**Figure 12.** (a)  $J$ - $V$  characteristics and (b) EQE spectra at 0 V bias of the CdS/Sb<sub>2</sub>Se<sub>3</sub> solar cells grown without and with the controlled addition of oxygen. The device with oxygen supplied only at the initial stage of the Sb<sub>2</sub>Se<sub>3</sub> film-grown process is denoted as F-Sb<sub>2</sub>Se<sub>3</sub>, while introducing oxygen only at the final stage is denoted as B-Sb<sub>2</sub>Se<sub>3</sub>. (c) Typical frequency dependence of the measured capacitance and (d)  $C^{-2}$  versus  $V$  curves for the two typical devices, measured at 100 kHz. (Reprinted with permission from reference [34]. Copyright 2015 John Wiley and Sons).

measured in the dark and under 100 mW cm<sup>-2</sup> simulated AM1.5G irradiation. The best device exhibited  $V_{oc}$  of 0.49 V,  $J_{sc}$  of 6.6 mA cm<sup>-2</sup>, and  $FF$  of 44.2%, corresponding to a power conversion efficiency of 1.43%. Despite the low efficiency, the aqueous solution process presents a green and low-cost strategy to build Sb<sub>2</sub>Se<sub>3</sub> thin film and Sb<sub>2</sub>Se<sub>3</sub> sensitized solar cells which merits further exploration and optimization.

**4.2.2. Vacuum-processed method.** In parallel, thermal evaporation was also applied to fabricate Sb<sub>2</sub>Se<sub>3</sub> thin films. Sb<sub>2</sub>Se<sub>3</sub> has a high vapor pressure (3.54 kPa at 600 °C) and congruent evaporation, suitable for a vacuum process. We first built a thermally evaporated Sb<sub>2</sub>Se<sub>3</sub> solar cell using CBD-deposited CdS as n-buffer layer and followed a superstrate structure (FTO/CdS/Sb<sub>2</sub>Se<sub>3</sub>/Au) (figure 9(a)) [32]. The device efficiency was 1.9% ( $V_{oc}$  = 300 mV,

$J_{sc}$  = 13.2 mA cm<sup>-2</sup>,  $FF$  = 48%, figure 9(b)). With an aging test, the cell performance increased mainly due to  $V_{oc}$  gain to which the p-n junction interface and diode quality enhancement might possibly have contributed. Admittance spectroscopy (AS), capacitance versus frequency (C-f) and voltage (C-V) and drive-level capacitance profiling (DLCP) were used to analyze the necessary parameters such as the doping density, bulk and surface defect density etc, for further optimization. The C-f test (figure 9(c)) reveals that deep defects having a very low-frequency response are likely to exist. The C-V and DLCP test (figure 9(d)) show that the doping densities via C-V and DLCP are almost identical, indicating that bulk defects and unfavorable band diagram are the main limiting factors for device performance.

In addition to superstrate configuration, Liu *et al* [33] designed a substrate Sb<sub>2</sub>Se<sub>3</sub> solar cell, analogous to CIGS-structure. They first deposited Sb<sub>2</sub>Se<sub>3</sub> film on fluorine-doped

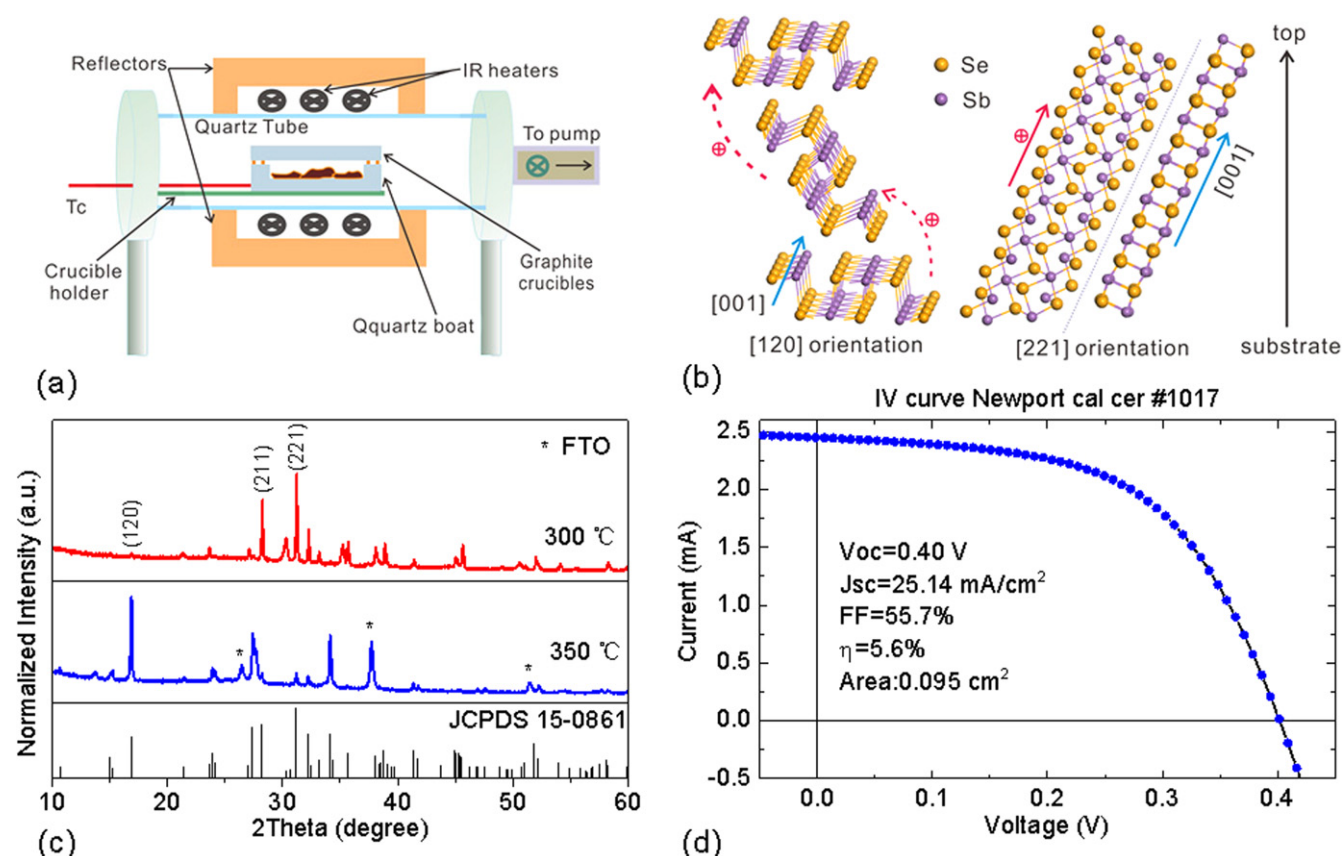


**Figure 13.** (a) The schematic diagram of RTE equipment for  $\text{Sb}_2\text{Se}_3$  film deposition. (b) Atomic structures of [120]- and [221]-oriented grains in  $\text{Sb}_2\text{Se}_3$ . The substrate is the CdS buffer layer on which the  $\text{Sb}_2\text{Se}_3$  ribbons grow. (c) XRD patterns of  $\text{Sb}_2\text{Se}_3$  film grown at different substrate temperature. The standard diffraction pattern for  $\text{Sb}_2\text{Se}_3$  (JCPDS 15-0861) is included for reference. (d)  $J$ - $V$  characteristics of the FTO/ $\text{CdS}/\text{Sb}_2\text{Se}_3/\text{Au}$  solar cell independently certified by the Newport Cooperation. (Reprinted with permission from Macmillan Publishers Ltd: *Nature* [19]. Copyright 2015).

tin oxide (FTO) by thermal evaporation, and then deposited CBD-processed CdS on the film. ZnO and ZnO:Al were sequentially sputtered and Au was evaporated to serve as the anode. In this way, the FTO/CdS/ $\text{Sb}_2\text{Se}_3$ /ZnO/ZnO:Al/Au structure (figure 10(a)) was constructed and thus achieved a 2.1% PCE, as shown in figure 10(b). The EQE curve (figure 10(d)) generally forms a quasi-triangle instead of a rectangle that is often seen in high-efficiency solar cells, indicating carrier collection losses both at the short and long wavelengths. Strong absorption by the CdS layer and the recombination losses of carriers at the back are likely to contribute to the EQE decline at the short-wavelength and long-wavelength region, respectively.

Based on the deep analysis of temperature-dependent vapor pressure of  $\text{Sb}_2\text{Se}_3$ , Sb and Se, one problem associated with the evaporation process is that large amounts of selenium vacancies ( $V_{\text{Se}}$ ) are generated due to the higher vapor pressure of Se rather than Sb. Selenium vacancies were n-type donors that not only reduce the effective p-type doping density of  $\text{Sb}_2\text{Se}_3$  film, but act as recombination centers trapping and annihilating photogenerated carriers. To diminish  $V_{\text{Se}}$ -related recombination loss, Leng *et al* [34] utilized a post-selenization process during thermal evaporation. Through a set of device physics experiments including biased EQE, admittance

(C-f), capacitance voltage (C-V) and C-V profiling measurements, we could conclude that an additional selenization step provided excess Se to compensate for the  $V_{\text{Se}}$  and hence increased the doping density and attenuated recombination loss. Meanwhile, selenization also helped in improving CdS/ $\text{Sb}_2\text{Se}_3$  heterojunction quality, thus increasing device  $V_{oc}$  and FF. As a result, our superstrate CdS/ $\text{Sb}_2\text{Se}_3$  solar cell exhibited significantly improved device performance compared to the control device without post-selenization (figure 11) and achieved an efficiency of 3.7%.

Later, this work progressed on the function of the controlled addition of oxygen during thermal evaporation of  $\text{Sb}_2\text{Se}_3$  films. Analogous to conventional CdS/CdTe solar cells, the defects at the CdS/ $\text{Sb}_2\text{Se}_3$  interface are believed to be serious and will diminish open-circuit voltage and fill factor in thermally evaporated  $\text{Sb}_2\text{Se}_3$  solar cells. Oxygen is introduced to check if interface defects can be passivated by setting a control device (C- $\text{Sb}_2\text{Se}_3$ ) and an oxygen-introduced device (O- $\text{Sb}_2\text{Se}_3$ ). With gradient levels of oxygen partial pressure, the beneficial effect of oxygen is fully recognized and an optimal condition is found at  $1.6\text{E}-3$  Pa. By further optimizing the procedure, i.e., introducing oxygen only in the initial stage of the  $\text{Sb}_2\text{Se}_3$  film deposition, but stopping the flux of oxygen for the deposition of the remaining  $\text{Sb}_2\text{Se}_3$  film, the best device

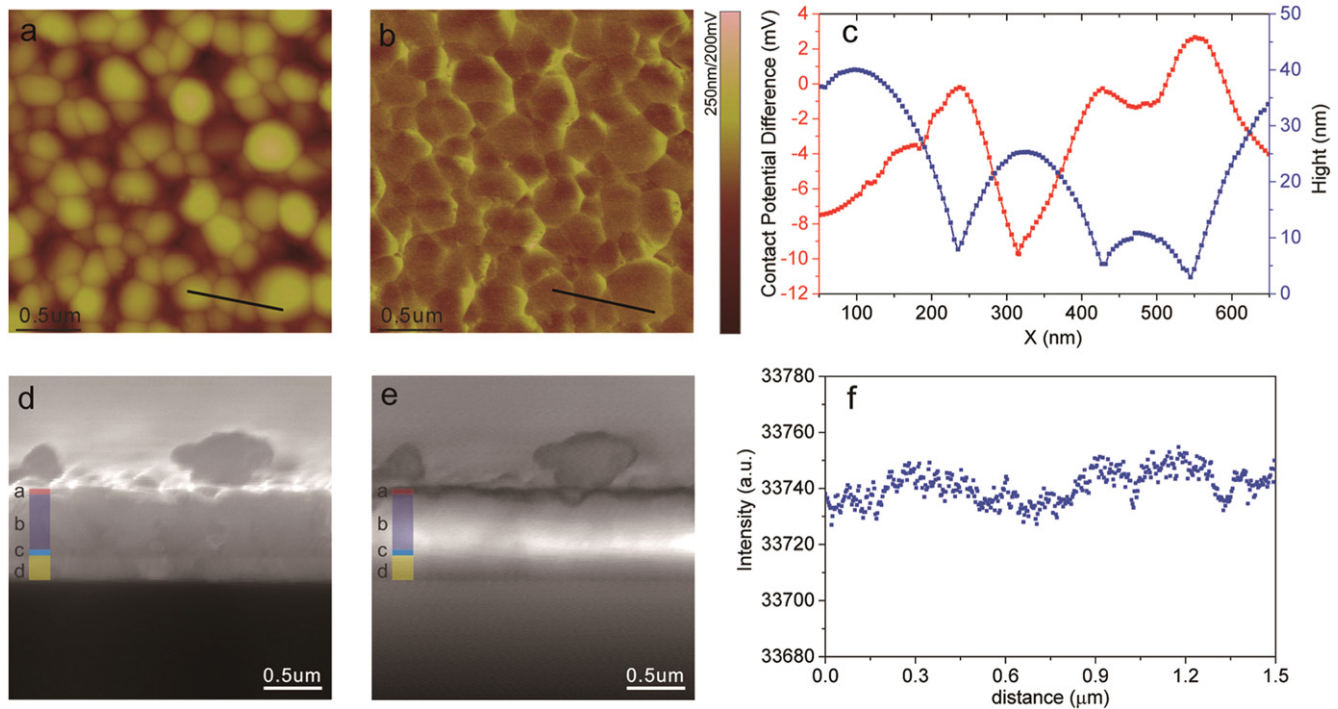


**Figure 14.** (a) Atomic force microscopy (AFM) and (b) scanned KPFM image of the device. (c) Contact potential difference (red) and height (blue) along the solid black lines drawn in panel (a) and (b). (d) Cross-sectional SEM and (e) EBIC image for the cleaved  $\text{Sb}_2\text{Se}_3$  device. For the colored legend, a is Au, b is  $\text{Sb}_2\text{Se}_3$ , c is CdS and d is FTO. (f) The intensity profiling along the dashed blue line is marked in (e). The scattering in signal intensity is negligible in the scanned  $1.5 \mu\text{m}$  length, which suggests a uniform photocurrent-collecting efficiency even across the GBs. (Reprinted with permission from Macmillan Publishers Ltd: *Nature* [19]. Copyright 2015).

**Table 2.** Cell efficiency table for  $\text{Sb}_2\text{Se}_3$  solar cells.

Cell structure		Efficiency (%)	Publication date	Reference
Sensitized solar cell	FTO/bulk- $\text{TiO}_2$ /mp- $\text{TiO}_2$ / $\text{Sb}_2\text{Se}_3$ /HTM/HTL/Au	3.21	2014	[27]
	FTO/bulk- $\text{TiO}_2$ /mp- $\text{TiO}_2$ / $\text{Sb}_2(\text{S}_x\text{Se}_{1-x})_3$ /HTM/HTL/Au	6.6	2014	[28]
	FTO/ $\text{TiO}_2$ / $\text{Sb}_2\text{Se}_3$ /CuSCN/Au	2.1	2014	[29]
Thin-film solar cell	TCO/CdS/ $\text{Sb}_2\text{Se}_{3-x}\text{S}_x$ : $\text{Sb}_2\text{O}_3$ /PbS	0.66	2009	[31]
	FTO/CdS/ $\text{Sb}_2\text{Se}_3$ /Au	1.9	2014	[32]
	FTO/CdS/ $\text{Sb}_2\text{Se}_3$ /ZnO/ZnO:Al/Au	2.1	2014	[33]
	FTO/ $\text{TiO}_2$ / $\text{Sb}_2\text{Se}_3$ /Au	2.26	2014	[15]
	FTO/CdS/ $\text{Sb}_2\text{Se}_3$ /Au	3.7	2014	[34]
	ITO/CdS/ $\text{Sb}_2\text{Se}_3$ /Au	4.8	2015	[35]
	FTO/CdS/ $\text{Sb}_2\text{Se}_3$ /Au	5.6	2015	[19]

exhibits an efficiency of 4.8% [35] while the control device exhibits 2.8%, showing nearly 71.4% enhancement in device efficiency. To further understand the effect of oxygen, a series of characterizations including biased EQE, secondary ion mass spectroscopy (SIMS),  $C-V$ , and AS are employed to analyze our samples. SIMS provides direct evidence that growing  $\text{Sb}_2\text{Se}_3$  films with oxygen have resulted in a higher amount of oxygen presented at the CdS/ $\text{Sb}_2\text{Se}_3$  interface, thus remedying defect states at the CdS/ $\text{Sb}_2\text{Se}_3$  interface. From the EQE curves in figure 12(b), O- $\text{Sb}_2\text{Se}_3$  exhibits considerable enhancement of photogenerated current in the short-wavelength, and from  $C-V$  curves in figure 12(d), and O- $\text{Sb}_2\text{Se}_3$  has a larger built-in voltage ( $V_{bi}$ ), indicating a better contact at CdS/ $\text{Sb}_2\text{Se}_3$ . Both the above are solid evidences that oxygen

helps passivate interface defects, thus leading to significant enhancement of device performance.

Besides the conventional thermal evaporation, we recently introduced the rapid thermal evaporation (RTE) method to produce high-quality  $\text{Sb}_2\text{Se}_3$  thin film using a tube furnace (MTI, Hefei, China, figure 13(a)).  $\text{Sb}_2\text{Se}_3$  powder was directly applied via evaporation under low vacuum pressure ( $\sim 8 \text{ mTorr}$ ), maintained by a mechanical pump. Once heated up,  $\text{Sb}_2\text{Se}_3$  powder evaporated and condensed on the substrate because of temperature gradient, forming the  $\text{Sb}_2\text{Se}_3$  film [19]. The deposition rate was as high as  $1 \mu\text{m min}^{-1}$ , much greater than regular thermal evaporation (typically  $0.01\text{--}0.1 \mu\text{m min}^{-1}$ ) or magnetron sputtering (typically  $0.01\text{--}0.05 \mu\text{m min}^{-1}$ ) and comparable to confined space sublimation (CSS). In 2015, we presented a device with orientation control by optimizing the



substrate temperature during the deposition of  $\text{Sb}_2\text{Se}_3$  film, using the as-mentioned RTE method. The Newport-certificated solar conversion efficiency was 5.6% ( $V_{\text{oc}} = 0.40$  V,  $J_{\text{sc}} = 25.14$  mA cm $^{-2}$ ,  $FF = 55.7\%$ , Area = 0.095 cm $^2$ ), as shown in figure 13(d). Moreover, this simple RTE technology can also be applied to fabricate  $\text{Bi}_2\text{S}_3$ -based thin-film solar cells with a preliminary power conversion efficiency of 0.75% [36], which could probably be extended to prepare other inorganic absorbers in the near future.

Furthermore, just through simple control of the substrate temperature during the RTE process, we could obtain  $\text{Sb}_2\text{Se}_3$  thin films with different orientations, specifically [120] orientation at 350 °C and [221] orientation at 300 °C. For [221] orientation, in figure 13(b), the charge carriers transfer more smoothly along the [001] chain where atoms correlate by covalent bonds, while they have to hop through the chains where atoms are correlated by Van der Waals force in [120] orientation. Through the careful investigation of the correlation between  $\text{Sb}_2\text{Se}_3$  film orientation and photovoltaic device performance, we concluded that the preferred orientation of  $\text{Sb}_2\text{Se}_3$  active layers is [211] orientation, which provides an efficient carrier transport and exhibits better device performance compared with [120] orientation.

To further confirm the defects at the GBs, Kelvin probe force microscopy (KPFM) and electron-beam-induced conductivity (EBIC) tests were performed. 2D topography spatial maps and the corresponding surface potentials of  $\text{Sb}_2\text{Se}_3$  thin films (figures 14(a), (b)) reveal that there is no correlation between the GBs. In an illustrative line scan crossing the GBs (figure 14(c)), the low surface potential difference between two grains indicates a lack of significant band bending and surface defects in the  $\text{Sb}_2\text{Se}_3$  films. The EBIC test (figures 14(e), (f)) shows the signal is uniform over multiple grains, excluding severe carrier recombination or an efficient current-collecting path presented at the GBs. The results were a good match with those of the KPFM. Both illustrate the GBs and grain interior are indistinguishable and the GBs are free of dangling bonds. Through theoretical analysis and experimental results, the  $\text{Sb}_2\text{Se}_3$  solar cell with oriented 1D ribbons and benign GBs is demonstrated. The device efficiencies of both sensitized and thin-film  $\text{Sb}_2\text{Se}_3$  solar cells are summarized in table 2. Clearly, the efficiency is soaring, confirming the bright future of  $\text{Sb}_2\text{Se}_3$  solar cells.

## 5. Conclusion

In this paper, we present a brief review of the basic properties of  $\text{Sb}_2\text{Se}_3$  and the relevant progress in photovoltaic application.  $\text{Sb}_2\text{Se}_3$  is low-toxic, low-cost, and earth-abundant, and the simple binary composition and single phase avoid complicated phase control during processing. Its large absorption coefficient, low temperature of crystal growth and high saturated vapor pressure make it suitable for thin-film solar cells, particularly when thermally deposited. Different deposition processes (solution/TE/RTE) and device structures (substrate/superstrate) are introduced to seek an optimal solution so that high efficiency can be achieved. The highest certificated

efficiency is 5.6% in a superstrate FTO/ $\text{CdS}/\text{Sb}_2\text{Se}_3/\text{Au}$  solar cell using the RTE method. Meanwhile, in comparison with the mainstream thin-film solar cells ( $\text{CdTe}$ , CIGS, etc), we are convinced that substantial enhancement can be achieved in  $V_{\text{oc}}$ ,  $J_{\text{sc}}$  and  $FF$ . Energy-band engineering can be introduced in the p-n junction to increase  $V_{\text{oc}}$  by methods like alloying and doping. The passivation of defects at the interface and the selection of appropriate n-buffer materials are vital means to reduce interface recombination and increase shunt resistance. More significantly, orientation control of  $\text{Sb}_2\text{Se}_3$  film is of paramount importance for this system, because of their unique 1D crystal structure. To conclude, in addition to further investigation of the fundamental optoelectronic properties of  $\text{Sb}_2\text{Se}_3$ , a systematic optimization of film quality, device structure and interfacial engineering is compulsory to approach a high power conversion efficiency of  $\text{Sb}_2\text{Se}_3$  thin-film solar cells. With further exploration on the listed aspects, we are confident that the device efficiency will be enhanced and more attention will be paid to the promising  $\text{Sb}_2\text{Se}_3$ -based thin-film solar cells.

## Acknowledgments

This work was supported by the director fund of Wuhan National Laboratory for Optoelectronics, 'National 1000 Young Talents' project and the National Natural Science Foundation of China (NSFC 61322401, 91433105, 21403078). The authors would like to thank the Analytical and Testing Center of HUST and the Center for Nanoscale Characterization and Devices of WNLO for the characterization support.

## References

- [1] 2014 Solibro Beats World Record for Solar Cells (Solibro Press) [www.pv-tech.org/news/hanergys\\_solibro\\_has\\_20.5\\_cigs\\_solar\\_cell\\_verified\\_by\\_nrel](http://www.pv-tech.org/news/hanergys_solibro_has_20.5_cigs_solar_cell_verified_by_nrel)
- [2] 2014 First Solar Builds the Highest Efficiency thin Film PV cell on Record *First Solar Press* <http://investor.firstsolar.com/releasedetail.cfm?ReleaseID=864426>
- [3] Kim J *et al* 2014 High efficiency  $\text{Cu}_2\text{ZnSn}(\text{S},\text{Se})_4$  solar cells by applying a double  $\text{In}_2\text{S}_3/\text{CdS}$  emitter *Adv. Mater.* **26** 7427–31
- [4] Sinsermsuksakul P *et al* 2014 Overcoming efficiency limitations of SnS-based solar cells *Adv. Energy Mater.* **4** 1400496
- [5] Septina W *et al* 2014 Thin film solar cell based on  $\text{CuSbS}_2$  absorber fabricated from an electrochemically deposited metal stack *Thin Solid Films* **550** 700–4
- [6] Yang B *et al* 2014  $\text{CuSbS}_2$  as a promising Earth-abundant photovoltaic absorber material: a combined theoretical and experimental study *Chem. Mater.* **26** 3135–43
- [7] Xue D-j *et al* 2015  $\text{CuSbSe}_2$  as a potential photovoltaic absorber material: studies from theory to experiment *Adv. Energy Mater.* **5** 1501203
- [8] Limpins el M *et al* 2014 An inversion layer at the surface of n-type iron pyrite *Energ. Environ. Sci.* **7** 1974



- [9] Kojima A *et al* 2009 Organometal halide perovskites as visible-light sensitizers for photovoltaic cells *J. Am. Chem. Soc.* **131** 6050–1
- [10] Huang X *et al* 2015 High-performance transition metal-doped Pt<sub>3</sub>Ni octahedra for oxygen reduction reaction *Science* **348** 1230–4
- [11] Dong Q *et al* 2015 Electron-hole diffusion lengths >175  $\mu\text{m}$  in solution-grown CH<sub>3</sub>NH<sub>3</sub>PbI<sub>3</sub> single crystals *Science* **347** 967–70
- [12] Venkatasubramanian R *et al* 2001 Thin-film thermoelectric devices with high room-temperature figures of merit *Nature* **413** 597–602
- [13] Zhang H *et al* 2009 Topological insulators in Bi<sub>2</sub>Se<sub>3</sub>, Bi<sub>2</sub>Te<sub>3</sub> and Sb<sub>2</sub>Te<sub>3</sub> with a single Dirac cone on the surface *Nat. Phys.* **5** 438–42
- [14] Kong P P *et al* 2014 Superconductivity in strong spin orbital coupling compound Sb<sub>2</sub>Se<sub>3</sub> *Sci. Rep-UK* **4** 6679
- [15] Zhou Y *et al* 2014 Solution-processed antimony selenide heterojunction solar cells *Adv. Energy Mater.* **4** 1301846
- [16] Madelung O 2004 *Semiconductor: Data Handbook* 3rd Ed. (New York: Springer)
- [17] Chen C *et al* 2015 Optical properties of amorphous and polycrystalline Sb<sub>2</sub>Se<sub>3</sub> thin films prepared by thermal evaporation *Appl. Phys. Lett.* **107** 043905
- [18] Shockley W *et al* 1961 Detailed balance limit of efficiency of p-n junction solar cells *J. Appl. Phys.* **32** 510
- [19] Zhou Y *et al* 2015 Thin-film Sb<sub>2</sub>Se<sub>3</sub> photovoltaics with oriented one-dimensional ribbons and benign grain boundaries *Nat. Photonics* **9** 409–15
- [20] Xue D-J *et al* 2015 Recent progress in material study and photovoltaic device of Sb<sub>2</sub>Se<sub>3</sub> *Acta Phys. Sin.* **64** 38406–038406
- [21] Deng Z *et al* 2009 Simple colloidal synthesis of single-crystal Sb–Se–S nanotubes with composition dependent band-gap energy in the near-infrared *Nano Lett.* **9** 2015–20
- [22] Zhai T *et al* 2010 Single-crystalline Sb<sub>2</sub>Se<sub>3</sub> nanowires for high-performance field emitters and photodetectors *Adv. Mater.* **22** 4530–3
- [23] Rajpure K Y *et al* 2000 Effect of Se source on properties of spray deposited Sb<sub>2</sub>Se<sub>3</sub> thin films *Mater. Chem. Phys.* **62** 169–74
- [24] El-Sayad E A 2008 Compositional dependence of the optical properties of amorphous Sb<sub>2</sub>Se<sub>3–x</sub>S<sub>x</sub> thin films *J. Non-cryst. Solids* **354** 3806–11
- [25] Guijarro N *et al* 2012 Toward antimony selenide sensitized solar cells: efficient charge photogeneration at spiro-OMeTAD/Sb<sub>2</sub>Se<sub>3</sub>/metal oxide heterojunctions *J. Phys. Chem. Lett.* **3** 1351–6
- [26] Lai Y *et al* 2012 Preparation and characterization of Sb<sub>2</sub>Se<sub>3</sub> thin films by electrodeposition and annealing treatment *Appl. Surf. Sci.* **261** 510–4
- [27] Choi Y C *et al* 2014 Sb<sub>2</sub>Se<sub>3</sub>-sensitized inorganic-organic heterojunction solar cells fabricated using a single-source precursor *Angew. Chem. Int. Ed.* **53** 1329–33
- [28] Choi Y C *et al* 2014 Efficient inorganic-organic heterojunction solar cells employing Sb<sub>2</sub>(S<sub>x</sub>/Se<sub>1–x</sub>)<sub>3</sub> graded-composition sensitizers *Adv. Energy Mater.* **4** 1301680
- [29] Ngo T T *et al* 2014 Electrodeposition of antimony selenide thin films and application in semiconductor sensitized solar cells *ACS Appl. Mater. Inter.* **6** 2836–41
- [30] Xia Z *et al* 2015 Generalized water-processed metal chalcogenide complexes: synthesis and applications *Chem. Mater.* **27** 8048–57
- [31] Messina S *et al* 2009 Antimony selenide absorber thin films in all-chemically deposited solar cells *J. Electrochem. Soc.* **156** H327–32
- [32] Luo M *et al* 2014 Thermal evaporation and characterization of superstrate CdS/Sb<sub>2</sub>Se<sub>3</sub> solar cells *Appl. Phys. Lett.* **104** 173904
- [33] Liu X *et al* 2014 Thermal evaporation and characterization of Sb<sub>2</sub>Se<sub>3</sub> thin film for substrate Sb<sub>2</sub>Se<sub>3</sub>/CdS Solar cells *ACS Appl. Mater. Inter.* **6** 10687–95
- [34] Leng M *et al* 2014 Selenization of Sb<sub>2</sub>Se<sub>3</sub> absorber layer: an efficient step to improve device performance of CdS/Sb<sub>2</sub>Se<sub>3</sub> solar cells *Appl. Phys. Lett.* **105** 083905
- [35] Liu X *et al* 2015 Improving the performance of Sb<sub>2</sub>Se<sub>3</sub> thin film solar cells over 4% by controlled addition of oxygen during film deposition *Prog. Photovoltaics* **23** 1828–36
- [36] Song H *et al* 2016 Rapid thermal evaporation of Bi<sub>2</sub>S<sub>3</sub> layer for thin film photovoltaics *Sol. Energ. Mat. Sol. C* **146** 1–7